

Majorana Flat Bands in the Vortex Line of Superconducting Weyl Semimetals

Zhicheng Zhang^{1,2,*} and Kou-Han Ma^{1,2}

¹International Center for Quantum Materials and School of Physics, Peking University, Beijing 100871, China

²Hefei National Laboratory, Hefei 230088, China

We find that there exist Majorana flat bands (MFBs) in the vortex line of superconducting (SC) Weyl semimetals which break time reversal symmetry. Since a Weyl semimetal can be regarded as Chern insulators stacked along one (z) direction, so we decompose the vortex bound states of SC Weyl semimetals into the vortex bound states of SC Chern insulators labelled by k_z . After calculating the topological phase diagram of the SC Chern insulators both analytically and numerically, we can explain the appearance of MFBs and determine the exact boundaries of them in SC Weyl semimetals. What's more, tuning the chemical potential or the pairing strength can result in the MFBs along the whole k_z axis. Based on the above understanding, we propose a k_z -dependent Z_2 Chern-Simons invariant to characterize the MFBs. Finally, if we further consider an attractive Hubbard interaction, the aforementioned SC Weyl semimetal and MFBs can be realized under appropriate parameters.

I. INTRODUCTION

Since the discovery that there is the effective p -wave superconductivity in the s -wave superconductor-TI heterostructure [1–3], the vortex bound states (VBSs) of superconducting (SC) topological materials [1, 4–33] and topological unconventional superconductors [34–44] have attracted increasing attentions from more and more researchers. Among all kinds of topological materials, the VBSs of SC Weyl semimetals show many exotic and intriguing properties [28, 45–63]. For example, for a SC Weyl semimetal breaking time reversal symmetry in the pair density wave state, there will be gapless chiral Majorana modes in the vortex line protected by an emergent second Chern number [60]. In contrast, a SC time reversal symmetric Weyl semimetal can host Majorana zero modes (MZMs) at the ends of the vortex line, and topological invariants are also proposed to characterize such MZMs [28, 62]. Besides, experimental technologies such as point contact [64] and selective ion sputtering [65] have also been developed to induce superconductivity into topological semimetals, which motivates further theoretical study about the VBSs of SC Weyl semimetals.

Majorana flat bands (MFBs) are zero energy flat bands in the BdG spectra of a superconductor. They are found in the study of VBSs of 3D spinless chiral superconductor of the ³He-A type, where the boundaries of the flat bands are determined by the locations of the two gapless points of the bulk spectra [66]. Then it is found that after considering the in-plane magnetic field, a chiral $p_x \pm ip_y$ -wave superconductor will become a gapless superconductor and host MFBs [67]. Later, MFBs are reported to appear in noncentrosymmetric superconductors [68, 69], d -wave superconductors [70], and SC Weyl semimetals [71]. Very recently, type-II Dirac semimetals are also revealed to possess hinge MFBs [72]. Although MFBs in SC topological materials are intensively studied, the MFBs in the VBSs of superconducting Weyl semimetals are less

explored [60, 73, 74].

Based on the above motivations, we study the VBSs of SC Weyl semimetals which break time reversal symmetry. We find that there are MFBs in the vortex line (along z direction), and we can tune the chemical potential μ or the pairing strength Δ to obtain the MFBs along the whole k_z axis. It is well known that a Weyl semimetal can be regarded as Chern insulators stacked along one (z) direction, so we understand the VBSs of SC Weyl semimetals by studying the VBSs of SC Chern insulators labelled by k_z . We calculate the topological phase diagram of the SC Chern insulators both analytically and numerically. A SC Weyl semimetal corresponds to a line in the topological phase diagram, where each point represents a SC Chern insulator. Thus, according to the phase diagram, we can determine the Chern numbers of SC Chern insulators which make up the SC Weyl semimetals. Since there will be MZMs in the vortex core of chiral topological superconductors with odd Chern numbers, the MZMs in certain range of k_z constitute MFBs. In this way, we can explain the appearance of MFBs and determine the exact boundary of them in the vortex line of SC Weyl semimetals. Based on such understanding, we further propose a k_z -dependent Z_2 Chern-Simons invariant to characterize the MFBs in the vortex line. Finally, we add the attractive Hubbard interaction into the Weyl semimetal, and mean field calculations can give the aforementioned SC Weyl semimetals with BCS pairing and the MFBs in the vortex line under appropriate parameters.

II. MODELS OF CHERN INSULATORS AND WEYL SEMIMETALS

We start with the model of a Chern insulator.

$$H_{\text{CI}}(\mathbf{k}) = [m + 2B(2 - \cos k_x - \cos k_y)]\sigma_3 + A \sin k_x \sigma_1 + A \sin k_y \sigma_2 \quad (1)$$

For the sake of concreteness, we set the parameters as $A = 1$ and $B = -0.5$ throughout this article. The properties of such a Chern insulator are well known. The bulk gap

* zhicheng.zhang1995@pku.edu.cn

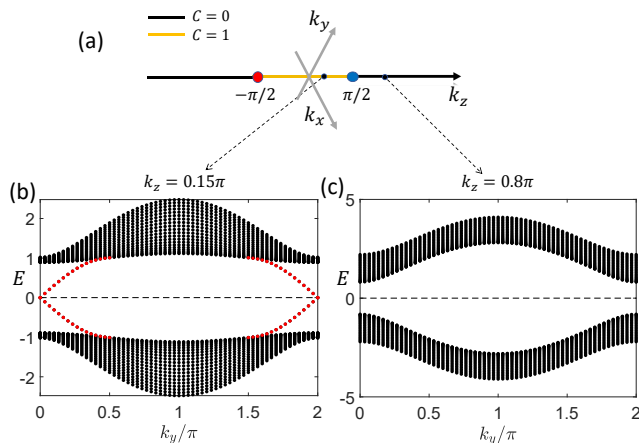


FIG. 1. The Weyl semimetal can be regarded as 2D insulators with different Chern numbers stacked along z direction. (a) The distribution of Weyl points. The red and blue points represent two Weyl points with opposite chirality. The Chern number for each insulator obtained at the fixed k_z is labelled on the k_z axis. (b) The spectra calculated with open boundary condition in x direction and periodic boundary condition in y direction for the 2D insulator at $k_z = 0.15\pi$. There is in gap edge states corresponding to $C = 1$. (c) The spectra calculated for the 2D insulator at $k_z = 0.8\pi$. There is no topological edge states due to $C = 0$.

closes at $m = 0$, $m = 2$, and $m = 4$, which are the three topological phase transition points. We can calculate the Chern number of this Chern insulator and obtain $C = 0$ for $m < 0$ or $m > 4$, $C = 1$ for $0 < m < 2$, and $C = -1$ for $2 < m < 4$.

Then we write down the corresponding model of a 3D time reversal symmetry breaking Weyl semimetal.

$$H_{\text{WSM}}(\mathbf{k}) = [2t_z \cos k_z + 2B_W(2 - \cos k_x - \cos k_y)]\sigma_3 + A_W \sin k_x \sigma_1 + A_W \sin k_y \sigma_2 \quad (2)$$

We have chosen the names of the parameters in the above Hamiltonian deliberately, so that parameters A_W , B_W , and $2t_z \cos k_z$ in Eq. (2) correspond to A , B , and m in Eq. (1), respectively. Since we have set $A = 1$ and $B = -0.5$ in Eq. (1), we set the parameters as $A_W = 1$, $B_W = -0.5$, and $t_z = 0.5$ in the model of the Weyl semimetal Eq. (2). Under this set of parameters, it is easy to find that the Weyl points obtained with gap closing condition are determined by $\cos k_z = 0$. Thus, the model Eq. (2) describes a Weyl semimetal with two Weyl points located at $(0, 0, \pm\pi/2)$ on the k_z axis. As shown in Fig. 1(a), the red point and blue point indicate the opposite chirality of the two Weyl points.

If we fix the value of k_z , we will obtain a 2D insulator ($k_z \neq \pm\pi/2$), in which we can define the Chern number. For $-\pi/2 < k_z < \pi/2$, we have $2t_z \cos k_z \in (0, 1)$. Because $2t_z \cos k_z$ corresponds to m in the model of Chern insulator Eq. (1), and $C = 1$ for $0 < m < 2$, we conclude that $C = 1$ for insulators at k_z with $-\pi/2 < k_z < \pi/2$ in the 3D Weyl semimetal, which is indicated by the yellow

line in Fig. 1(a). In contrast, for $-\pi < k_z < -\pi/2$ or $\pi/2 < k_z < \pi$, we have $2t_z \cos k_z \in (-1, 0)$. Because $C = 0$ for $m < 0$ in the model of Chern insulator Eq. (1), we conclude that $C = 0$ for insulators at k_z with $-\pi < k_z < -\pi/2$ or $\pi/2 < k_z < \pi$ in the Weyl semimetal, which corresponds to the black lines in Fig. 1(a). The above arguments are verified by numerical calculations. For example, we choose open boundary condition in x direction and periodic boundary condition in y direction for the 2D insulator at $k_z = 0.15\pi$, and the spectra are shown in Fig. 1(b). It is noticeable that there are non-trivial in-gap edge states corresponding to $C = 1$. On the other hand, when we fix $k_z = 0.8\pi$, calculations with open boundary condition in x direction lead to the spectra shown in Fig. 1(c), where we cannot find topological edge states. Thus, we have shown clearly that the Weyl semimetal can be viewed as insulators with different Chern numbers stacked in z direction, and there is the direct correspondence between the model of the Chern insulator Eq. (1) and the model of the Weyl semimetal Eq. (2).

Above discussions focus on the properties of normal state Weyl semimetals. To study the VBSs of SC Weyl semimetals, we have to consider the pairing terms. Thus, we consider the following BdG Hamiltonian describing a SC Weyl semimetal with BCS pairing under the basis $\Psi_{\mathbf{k}}^\dagger = (c_{\mathbf{k}\uparrow}^\dagger, c_{\mathbf{k}\downarrow}^\dagger, c_{-\mathbf{k}\uparrow}, c_{\mathbf{k}\uparrow})$.

$$H_{\text{BdG}}(\mathbf{k}) = \begin{pmatrix} H_N(\mathbf{k}) - \mu & \tilde{\Delta} \\ \tilde{\Delta}^\dagger & \mu - H_N^*(-\mathbf{k}) \end{pmatrix}. \quad (3)$$

Here $H_N(\mathbf{k})$ refers to the normal state Hamiltonian of 2D Chern insulators or 3D Weyl semimetals, and $\tilde{\Delta} = \Delta i\sigma_2$. To calculate the VBSs of SC Weyl semimetals, we have to add a π -flux inserted into the superconductor (along z direction). Such a π -flux line can be described by attaching the phase $e^{i\theta}$ ($\theta = \arctan y/x$) to the pairing potential. Obviously, the vortex line breaks the translation symmetry in x and y directions but preserves the translation symmetry in z direction. Therefore, we can choose the open boundary conditions in x and y directions and calculate the VBSs for each k_z . Besides, we assume that the pairing potential at the vortex core is $\Delta = 0$, and $\Delta(\mathbf{r}) = \Delta e^{i\theta}$ on other lattice sites.

III. THE TOPOLOGICAL PHASE DIAGRAM OF SUPERCONDUCTING CHERN INSULATORS

In the above section, we have demonstrated the close connections between the Chern insulator Eq. (1) and the Weyl semimetal Eq. (2). As a matter of fact, it turns out that we can obtain the VBSs of SC Weyl semimetals from the VBSs of SC Chern insulators. Because the VBSs of SC Chern insulators are determined by their topological properties, in this section we will delve into the topological phase diagram of SC Chern insulator Eq. (3), where $H_N(\mathbf{k})$ refers to the Chern insulators described by Eq. (1).

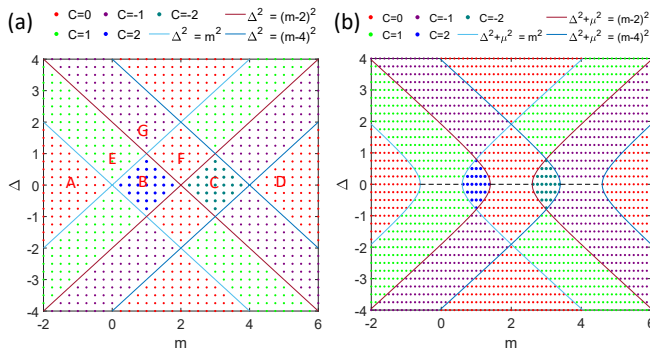


FIG. 2. (a) The topological phase diagram of the SC Chern insulator Eq. (3) with $\mu = 0$. As indicated in the legend, regions with different Chern numbers are filled with points with different colors. The expressions of three pairs of phase boundaries are also given in the legend. (b) The topological phase diagram of the SC Chern insulator Eq. (3) with $\mu = 0.6$. The gray dashed lines within the regions $m \in (-\mu, \mu)$, $m \in (2 - \mu, 2 + \mu)$, and $m \in (4 - \mu, 4 + \mu)$ at $\Delta = 0$ contain the physics that the chemical potential is tuned to the conduction band, and zero pairing strength leads to gapless spectra. Thus, we cannot define Chern number for points on these gray dashed lines.

A. The $\mu = 0$ case

For clarity, we first consider the $\mu = 0$ case. The topological phase diagram of the continuous version of Eq. (3) is analyzed in a seminal paper about SC Chern insulators [75]. Analogous to the arguments in this seminal paper, we will derive the topological phase diagram by checking the topological transitions at the gapless phase boundaries. First we give the BdG Chern numbers for the points on the $\Delta = 0$ line. When $\Delta = 0$, the BdG Hamiltonian Eq. (3) is decoupled into an upper left 2×2 block and a lower right 2×2 block. It is easy to find that insulators of the two blocks have the same Chern number. Thus, compared to the Chern number of the Chern insulators in Eq. (1), the BdG Chern number of SC Chern insulators at $\Delta = 0$ simply doubles. As shown in Fig. 2(a), we obtain $C = 0$ for $m < 0$ or $m > 4$ (region A and region D), $C = 2$ for $0 < m < 2$ (region B), and $C = -2$ for $2 < m < 4$ (region C).

The Chern number of a SC Chern insulator will not change unless the bulk gap closes and reopens, so we determine the topological phase boundaries from gap closing conditions and derive the BdG Chern numbers in other regions by observing the changes of Chern number around the phase boundaries. The bulk spectra of the SC Chern insulator Eq. (3) are $E = \pm \sqrt{(\sin^2 k_x + \sin^2 k_y) + (\Delta \pm m(\mathbf{k}))^2}$, in which we have used the notation $m(\mathbf{k}) = m - (2 - \cos k_x - \cos k_y)$. The bulk gap closing conditions require $\sin k_x = 0$, $\sin k_y = 0$, and $\Delta \pm m(\mathbf{k}) = 0$. According to the three equations, we can obtain the topological phase boundaries, and the results are summarized in Table I. When $\Delta = \pm m$, the

| (k_x, k_y) | $m(\mathbf{k}) = m - (2 - \cos k_x - \cos k_y)$ | Δ^2 |
|----------------------|---|-------------|
| $(0, 0)$ | m | m^2 |
| $(0, \pi), (\pi, 0)$ | $m - 2$ | $(m - 2)^2$ |
| (π, π) | $m - 4$ | $(m - 4)^2$ |

TABLE I. Topological phase boundaries determined from the bulk gap closing condition (the $\mu = 0$ case). When $\Delta = \pm m$, the gapless point is $(0, 0)$. When $\Delta = \pm(m - 2)$, the gapless points are $(0, \pi)$ and $(\pi, 0)$. When $\Delta = \pm(m - 4)$, the gapless point is (π, π) .

gapless point is $(0, 0)$. If $\Delta = \pm(m - 2)$, the bulk gap closes at two points $(0, \pi)$ and $(\pi, 0)$. For $\Delta = \pm(m - 4)$, the bulk gap closes at (π, π) . Otherwise, the bulk spectra are fully gapped, and there is no topological phase transition. Now we derive the BdG Chern numbers in regions where $\Delta \neq 0$. As shown in Fig. 2(a), region E is adjacent to both region A and region B. The phase boundary between region E and region A is $\Delta = -m$, which corresponds to only one gapless point $(0, 0)$, so the change of Chern number is ± 1 . Because the Chern number in region A is $C = 0$, we have $C = \pm 1$ in region E. On the other hand, the phase boundary between region E and region B is $\Delta = m$, corresponding to one gapless point $(0, 0)$, so the change of Chern number is also ± 1 . We know that $C = 2$ in region B, so in region E we have $C = 1$ or $C = 3$. Combining the two results, we conclude that the Chern number in region E is $C = 1$. We can also obtain the Chern number in region F in a very similar way. The phase boundary between region B and region F is $\Delta = -(m - 2)$, and bulk gap closes at two points $(0, \pi)$ and $(\pi, 0)$. We thus expect that the change of Chern number is ± 2 . Considering $C = 2$ in region B, it could be $C = 0$ or $C = 4$ in region F. Given that the phase boundary between region F and region C also corresponds to two gapless points, the change of Chern number is also ± 2 . Because $C = -2$ in region C, we have $C = 0$ or $C = -4$ in region F. Taking the two aspects into account, we conclude $C = 0$ in region F. Similarly, we can analytically obtain the Chern numbers in all regions of the topological phase diagram Fig. 2(a).

The analytical results above can be verified through numerical calculations. We adopt the following formula to calculate the Chern number [59, 76].

$$C = \int \frac{d\mathbf{k}}{2\pi} \text{Im} \sum_{a,b} \frac{\langle u_a | \partial_{k_x} H | u_b \rangle \langle u_b | \partial_{k_y} H | u_a \rangle - (k_x \leftrightarrow k_y)}{(E_a - E_b)^2}. \quad (4)$$

For an insulator with N bands in total and M bands occupied, the summation of the index a is from 1 to M (occupied bands), and the summation of the index b is from $M + 1$ to N (the unoccupied bands). Applying this formula to our SC Chern insulator, we obtain the Chern numbers for colored dots in the topological phase diagram Fig. 2(a). Obviously, the numerical results are consistent with the analytical results, and points with different colors are separated by the analytical phase boundaries.

B. The $\mu \neq 0$ case

Then we calculate the topological phase diagram for the $\mu \neq 0$ case. We still calculate the topological phase

$$E = \pm \sqrt{(\sin^2 k_x + \sin^2 k_y) + \Delta^2 + m(\mathbf{k})^2 + \mu^2} \pm 2\sqrt{(\Delta^2 + \mu^2)m^2(\mathbf{k}) + \mu^2(\sin^2 k_x + \sin^2 k_y)}, \quad (5)$$

where $m(\mathbf{k}) = m - (2 - \cos k_x - \cos k_y)$. When we consider the case $m^2(\mathbf{k}) - \mu^2 \geq 0$, the gap closing conditions lead to $\sin^2 k_x + \sin^2 k_y + \Delta^2 + \mu^2 - m^2(\mathbf{k}) = 0$ and $(\sin^2 k_x + \sin^2 k_y)(m^2(\mathbf{k}) - \mu^2) = 0$. The two equations can be transformed to another three equations $\sin k_x = 0$, $\sin k_y = 0$, and $\Delta^2 + \mu^2 - m^2(\mathbf{k}) = 0$. We can obtain the topological phase boundaries from the equations above, and the results are given in Table II. There are three pairs of phase boundaries, and all of them are hyperbolas. As a concrete example, the topological phase diagram

| (k_x, k_y) | $m(\mathbf{k}) = m - (2 - \cos k_x - \cos k_y)$ | $\Delta^2 + \mu^2$ |
|----------------------|---|--------------------|
| $(0, 0)$ | m | m^2 |
| $(0, \pi), (\pi, 0)$ | $m - 2$ | $(m - 2)^2$ |
| (π, π) | $m - 4$ | $(m - 4)^2$ |

TABLE II. Topological phase boundaries determined from the bulk gap closing condition (the $\mu \neq 0$ case). When $\Delta^2 + \mu^2 = m^2$, the gapless point is $(0, 0)$. When $\Delta^2 + \mu^2 = (m - 2)^2$, the gapless points are $(0, \pi)$ and $(\pi, 0)$. When $\Delta^2 + \mu^2 = (m - 4)^2$, the gapless point is (π, π) .

for the $\mu = 0.6$ case is shown in Fig. 2(b). Points with all kinds of colors calculated numerically with the formula Eq. (4) have different Chern numbers, which is demonstrated in the legend of Fig. 2(b). Three pairs of hyperbolas with different colors are the aforementioned topological phase boundaries, and the explicit expressions of them are also given in the legend. We notice that the points with different Chern numbers are separated by the analytical topological phase boundaries, and numerical results are consistent with the analytical phase boundaries. Compared to the topological phase diagram of the $\mu = 0$, we find that for regions around $\Delta = 0$, the deformed phase boundaries enlarge the regions with Chern number $C = 1$ (region E in Fig. 2(a)) and $C = -1$ and make regions with $C = 2$ (region B in Fig. 2(a)) and $C = -2$ (region C in Fig. 2(a)) to shrink. In fact, if we increase μ , the regions with $C = 2$ and $C = -2$ will get smaller.

It is worthwhile to point out that the above topological phase boundaries are calculated with the assumption $m^2(\mathbf{k}) - \mu^2 \geq 0$. Now we discuss the physics under the condition $m^2(\mathbf{k}) - \mu^2 < 0$. It turns out that this condition corresponds to three gray dashed lines within the regions $m \in (-\mu, \mu)$, $m \in (2 - \mu, 2 + \mu)$, and $m \in (4 - \mu, 4 + \mu)$ at $\Delta = 0$ in Fig. 2(b). In fact, when the condition $m^2(\mathbf{k}) - \mu^2 < 0$ is satisfied, the chemical potential is tuned

boundaries by applying the gap closing conditions. Since $\mu \neq 0$, the bulk spectra now become

to the conduction band, so zero paring strength ($\Delta = 0$) will lead to gapless spectra. Thus, we cannot define Chern number for points on this line. However, these gapless spectra don't correspond to topological phase transitions, because these gapless points are on the Fermi surface, and the dispersion around each point is not a Dirac cone. As shown in Fig. 2(b), the two regions separated by a gray line have the same Chern number.

IV. MAJORANA FLAT BANDS IN THE VORTEX LINE OF SUPERCONDUCTING WEYL SEMIMETALS

In this section we will present the VBSs of SC time reversal symmetry breaking Weyl semimetals Eq. (3), in which $H_N(\mathbf{k})$ refers to the normal state Weyl semimetal Eq. (2). As shown in Fig. 3, we have calculated the VBSs of SC Weyl semimetals under three sets of parameters, which illustrates the universality of the appearance of MFBs. We also understand these MFBs and determine the boundaries of them from the topological phase diagrams of the corresponding SC Chern insulators.

To be specific, Fig. 3(a) shows the VBSs of SC Weyl semimetals with $\mu = 0$ and $\Delta = 0.5$. The states close to the Fermi energy $E = 0$ are colored red to make them noticeable. We find that there are two pieces of zero energy flat bands (the MFBs) enclosed by the blue dashed boundaries ($k_z = \pm \frac{2\pi}{3}$ and $k_z = \pm \frac{\pi}{3}$), which are obtained from the topological phase diagram of the corresponding SC Chern insulators in Fig. 3(d). Although it seems that there is finite discrepancy between the blue dashed boundaries and the real boundaries of the MFBs, it is, in fact, due to the finite size effect. Some supplementary numerical results are given in the appendix to illustrate that as we increase the lattice size, the real boundaries will approach the blue dashed boundaries. Now we discuss how to understand the appearance of MFBs and obtain the exact boundaries of them from the topological phase diagram Fig. 3(d). Because there is a direct correspondence between the Chern insulator Eq. (1) and the Weyl semimetal Eq. (2) by identifying m in the Chern insulator with $2t_z \cos k_z$ in the Weyl semimetal, every k_z in the Weyl semimetal gives a Chern insulator, and the Weyl semimetal can be described by the thick orange line in the topological phase diagram Fig. 3(d). We have

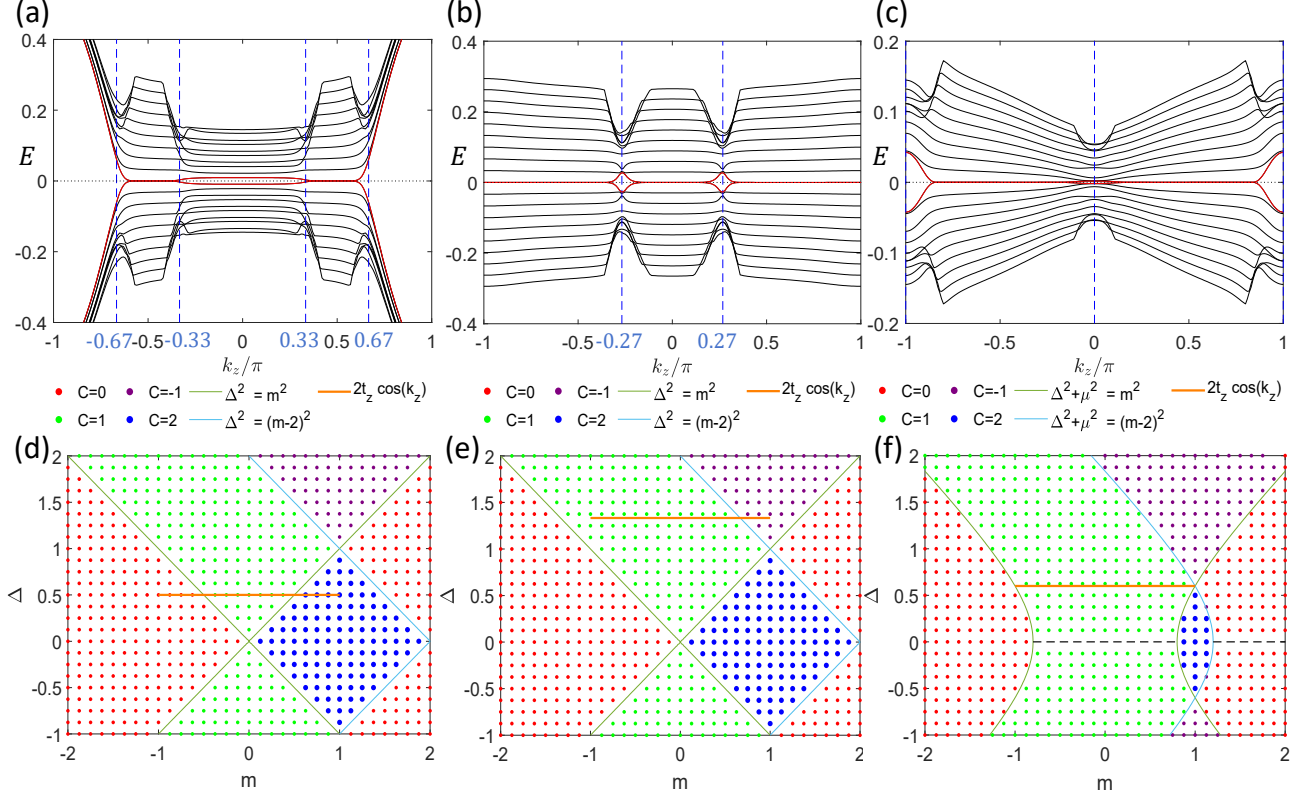


FIG. 3. The VBSs of SC Weyl semimetal and the understanding from the topological phase diagram of corresponding SC Chern insulators. (a) The VBSs of SC Weyl semimetals with $\mu = 0$ and $\Delta = 0.5$. (b) The VBSs of SC Weyl semimetals with $\mu = 0$ and $\Delta = 4/3$. (c) The VBSs of SC Weyl semimetals with $\mu = 0.8$ and $\Delta = 0.6$. The dashed blue lines in the sub-figures (a), (b), and (c) are the analytical (exact) boundaries of the MFBs. (d) The topological phase diagram of SC Chern insulator Eq. (1) with $\mu = 0$. The thick orange line represents the SC Weyl semimetal in the sub-figure (a). (e) The topological phase diagram of SC Chern insulator with $\mu = 0$. The thick orange line represents the SC Weyl semimetal in the sub-figure (b). (f) The topological phase diagram of SC Chern insulator with $\mu = 0.8$. The thick orange line represents the SC Weyl semimetal in the sub-figure (c).

set $t_z = 0.5$, so $2t_z \cos k_z \in [-1, 1]$, which is the range of the x coordinate of the orange line. On the other hand, since we are studying the VBSs of a SC Weyl semimetal with $\Delta = 0.5$, the y coordinate of the orange line is $\Delta = 0.5$. The orange line intersects the topological phase boundaries $\Delta^2 = m^2$ at $(0.5, 0.5)$ and $(-0.5, 0.5)$. Thus, the $C = 1$ part (the green region) of the orange line is within the range $m \in (-0.5, 0.5)$. Then the condition $2t_z \cos k_z \in (-0.5, 0.5)$ gives rise to $k_z \in (-2\pi/3, -\pi/3)$ and $k_z \in (\pi/3, 2\pi/3)$. Because the chiral superconductor with odd Chern number will host Majorana zero modes in the vortex line [75, 77], we conclude that for $k_z \in (-2\pi/3, -\pi/3)$ and $k_z \in (\pi/3, 2\pi/3)$, the corresponding 2D Chern insulators have Chern number $C = 1$, and the Majorana zero modes at the two ranges of k_z will constitute the MFBs. Obviously, the exact boundaries of the MFBs are $k_z = \pm\pi/3$ and $k_z = \pm 2\pi/3$, which gives the blue dashed boundaries in Fig. 3(a).

The MFBs in Fig. 3(a) occupy a part of k_z axis, and we now analyze the MFB occupying the whole k_z axis in Fig. 3(b), which shows the VBSs of SC Weyl semimetals with $\mu = 0$ and $\Delta = 4/3$. Such a SC Weyl semimetal is

described by the thick orange line in Fig. 3(e). In this case, the Chern numbers for SC insulators obtained by fixing k_z in the SC Weyl semimetals are either $C = 1$ or $C = -1$. However, the orange line intersects the topological phase boundary $\Delta = -(m-2)$ at $(2/3, 4/3)$, where the spectrum of the SC Chern insulator is gapless, and we cannot define the BdG Chern number. $m = 2/3$ corresponds to $2t_z \cos k_z = 2/3$, and we obtain $k_z = \arccos 2/3 \approx \pm 0.27\pi$. Thus, for SC insulators obtained at $k_z \neq 0.27\pi$ in the SC Weyl semimetal, the BdG Chern numbers are odd, and the Majorana zero modes in the vortex line make up the MFB. At $k_z = \pm 0.27\pi$, the Chern number is ill-defined, and there is no reason that we should obtain zero modes. So we find there is discontinuity of the MFB at $k_z = \pm 0.27\pi$. In fact, if we increase the lattice size, the boundaries of MFBs will approach $k_z = \pm 0.27\pi$, and there will be less discontinuity in the MFBs.

The MFB on the whole k_z axis in Fig. 3(b) is obtained by tuning the pairing strength Δ , and we can also obtain the MFB on the whole k_z by changing the chemical potential μ . As shown in Fig. 3(c), there is MFB on the whole k_z axis in the VBSs of SC Weyl semimetal with $\mu = 0.8$

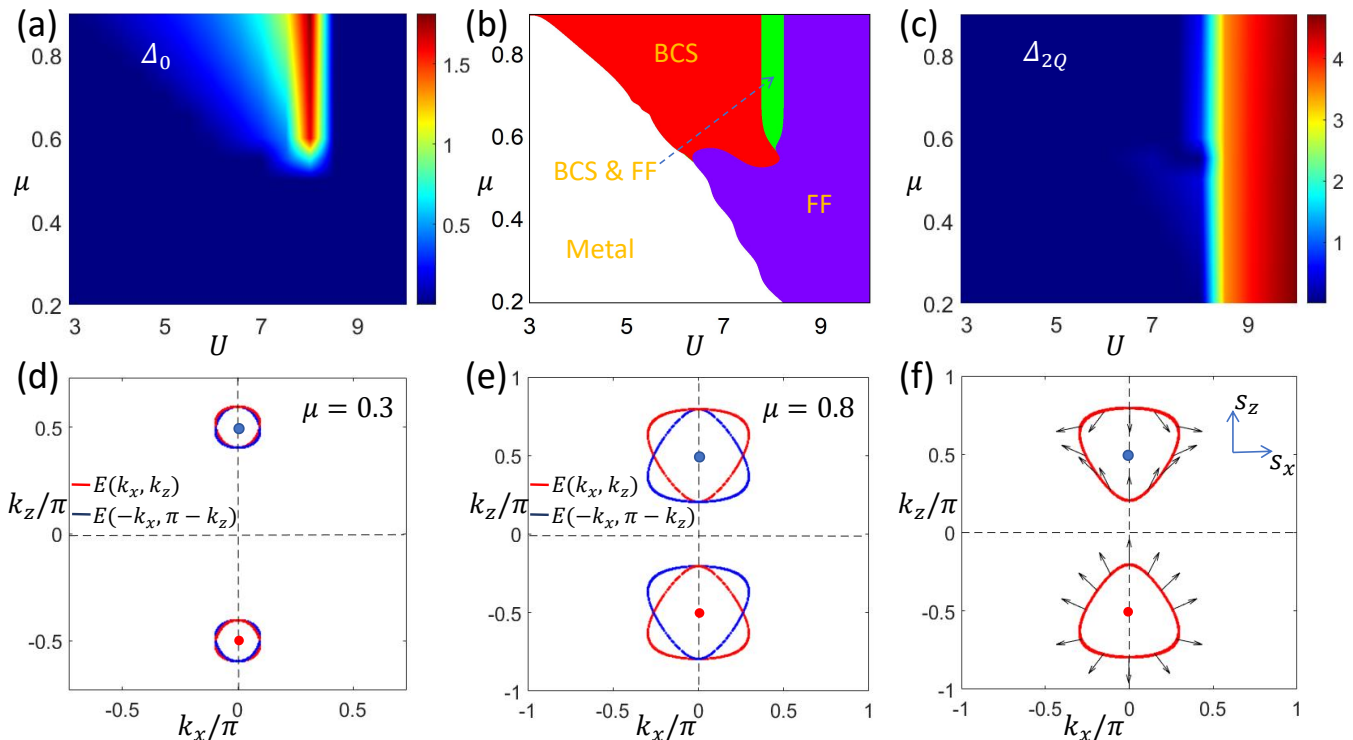


FIG. 4. The sub-figures (a) and (c) are the distributions of parameters Δ_0 and Δ_{2Q} in the $U - \mu$ space, respectively. Combining (a) and (c), we can obtain the phase diagram (b) of the model of Weyl semimetal with attractive Hubbard interaction. The sub-figures (d) and (e) show the Fermi surfaces and their particle-hole counterparts of the normal state Weyl semimetal at $\mu = 0.3$ and $\mu = 0.8$ (with $k_y = 0$), respectively. (f) shows the Fermi surface of the Weyl semimetal at $\mu = 0.8$ and the spin textures on it ($k_y = 0$).

and $\Delta = 0.6$, which is represented by the thick orange line in Fig. 3(f). Similar to the discontinuity in the MFBs in Fig. 3(b), there is also such discontinuity at $k_z = 0$ and $k_z = \pm\pi$, which are the boundaries of the MFBs that can be obtained from the topological phase diagram Fig. 3(f). Although there is significant distance between the real boundaries and the exact boundaries, when we increase the lattice size, the real boundaries will approach the exact boundaries. As shown in Fig. 3(f), the orange line intersects the topological phase boundaries $\Delta^2 + \mu^2 = m^2$ at $(-1, 0.6)$ and $(1, 0.6)$. The intersections at $m = 1$ and $m = -1$ corresponds to $k_z = 0$ and $k_z = \pm\pi$, respectively. Thus, if $k_z \neq 0$ or $k_z \neq \pm\pi$, the corresponding 2D SC Chern insulators have Chern number $C = 1$, and the Majorana zero modes in the vortex line constitute the MFB on the k_z axis. For $k_z = 0$ and $k_z = \pm\pi$, the spectra of SC Chern insulators are gapless, and there is no well-defined odd Chern number, so there could be vortex spectra without zero energy states, resulting in the discontinuity of the MFB at $k_z = 0$ and $k_z = \pm\pi$ in Fig. 3(c).

V. REALIZING SUPERCONDUCTING WEYL SEMIMETALS BY CONSIDERING ATTRACTIVE INTERACTIONS

Above discussions are based on the BdG Hamiltonian Eq. (3), in which the pairing term is added by hand. A natural question arises that how can we obtain such a pairing term. In the following texts, we will show that under appropriate parameters, the mean field approach can give the BCS pairing from the Weyl semimetal with attractive Hubbard interaction.

$$H_{\text{int}} = \sum_{\mathbf{k}} \psi^\dagger(\mathbf{k})(H_{\text{WSM}}(\mathbf{k}) - \mu)\psi(\mathbf{k}) - \frac{U}{V} \sum_{\mathbf{q}} \sum_{\mathbf{k}} \sum_{\mathbf{k}'} c_{\mathbf{k}'+\mathbf{q},\uparrow}^\dagger c_{-\mathbf{k}',\downarrow}^\dagger c_{-\mathbf{k},\downarrow} c_{\mathbf{k}+\mathbf{q},\uparrow}. \quad (6)$$

As shown in Fig. 4(f), the Fermi surfaces of the normal state Weyl semimetal consist of two closed circles around two Weyl points. Thus, the pairing with momentum $\mathbf{q} = \mathbf{0}$ and $\mathbf{q} = 2\mathbf{Q}$ may dominate, where $\mathbf{Q} = (0, 0, \pi/2)$ is the location of the Weyl point. $\mathbf{q} = \mathbf{0}$ corresponds to the BCS pairing between two Weyl cones, while $\mathbf{q} = 2\mathbf{Q}$ corresponds to the Fulde-Ferrell (FF) pairing within each Weyl cone [78]. So we keep only $\mathbf{q} = \mathbf{0}$ and $\mathbf{q} = 2\mathbf{Q}$ terms in the summation of \mathbf{q} in Eq. (6).

To apply the mean field approximation, we choose the

order parameters as $\Delta_{\mathbf{q}} = -\frac{U}{V} \sum_{\mathbf{k}} \langle c_{-\mathbf{k},\downarrow} c_{\mathbf{k}+\mathbf{q},\uparrow} \rangle$, where \mathbf{q} could be $\mathbf{0}$ or $2\mathbf{Q}$. When Δ_0 coexists with $\Delta_{2\mathbf{Q}}$, we cannot write the model in the form of a BdG Hamiltonian under the basis $\Psi^\dagger(\mathbf{k}) = (c_{\mathbf{k},\uparrow}^\dagger, c_{\mathbf{k},\downarrow}^\dagger, c_{-\mathbf{k},\uparrow}, c_{-\mathbf{k},\downarrow})$ with \mathbf{k} in the full Brillouin zone. Because the wave-vector $2\mathbf{Q}$ in the FF pairing $\Delta_{2\mathbf{Q}}$ is along z direction, we consider the Brillouin zone folded in z direction with $k_x, k_y \in (-\pi, \pi]$ and $k_z \in (0, \pi]$. The new basis considering the folded Brillouin zone (FBZ) is $\Psi^\dagger(\mathbf{k}) = (\tilde{c}_{\mathbf{k}}^\dagger, \tilde{c}_{\mathbf{k}+2\mathbf{Q}}^\dagger, \tilde{c}_{-\mathbf{k}}, \tilde{c}_{-\mathbf{k}-2\mathbf{Q}})$, where we have defined $\tilde{c}_{\mathbf{k}}^\dagger = (c_{\mathbf{k},\uparrow}^\dagger, c_{\mathbf{k},\downarrow}^\dagger)$. Under the new basis, the Hamiltonian now takes the following form

$$H = \frac{V}{U} |\Delta_0|^2 + \frac{V}{U} |\Delta_{2\mathbf{Q}}|^2 + \frac{1}{2} \sum_{\mathbf{k}} \text{Tr} H_N(\mathbf{k}) + \frac{1}{2} \sum_{\mathbf{k} \in \text{FBZ}} \Psi^\dagger(\mathbf{k}) H_{\text{BdG}}(\mathbf{k}) \Psi(\mathbf{k}), \quad (7)$$

in which the explicit form of $H_{\text{BdG}}(\mathbf{k})$ is given in Eq. (A10) in the appendix. After writing down the BdG Hamiltonian, according to the definition of the order parameters Δ_0 and $\Delta_{2\mathbf{Q}}$, we can derive the self-consistent gap equations, which are Eq. (A13) and Eq. (A14) in the appendix.

Then the phase diagram in the $\mu - U$ space can be obtained by solving the self-consistent gap equations under various parameters, and the results are shown in Fig. 4(a)-(c). Fig. 4(a) and (c) show the magnitude of Δ_0 and $\Delta_{2\mathbf{Q}}$ in the $\mu - U$ space, respectively. Combining the results in Fig. 4(a) and (c), we can obtain the phase diagram Fig. 4(b). In the BCS phase (the red region), Δ_0 dominates, and we have $|\Delta_0| > 1 \times 10^{-4}$ and $|\Delta_{2\mathbf{Q}}| < 1 \times 10^{-4}$. In contrast, $\Delta_{2\mathbf{Q}}$ in the FF phase (the purple region) dominates, and $|\Delta_0| < 1 \times 10^{-4}$ and $|\Delta_{2\mathbf{Q}}| > 1 \times 10^{-4}$. The BCS phase and FF phase coexist in the green region, where $|\Delta_0| > 1 \times 10^{-4}$ and $|\Delta_{2\mathbf{Q}}| > 1 \times 10^{-4}$. When μ and U are small (the white region), both the magnitude of Δ_0 and $\Delta_{2\mathbf{Q}}$ are negligibly small, so there is no pairing, and it is the normal-state metal phase. First, we notice that as we increase μ , we need a smaller U to obtain a SC phase. Since the low-energy normal state physics is described by a 3D Weyl cone, straightforward calculations give the density of states (DOS) $g(E) \propto E^2$. Thus, when we increase μ , the DOS at the Fermi surface gets larger, which will provide more electrons for forming Cooper pairs, so we need a smaller U to arrive at the SC phase.

There are still other remarkable features in the phase diagram Fig. 4(b), and we will analyze them one by one. First, the FF pairing is favored for smaller μ , while the BCS pairing is favored for greater μ . To understand this, we compare the Fermi surfaces in Fig. 4(d) with $\mu = 0.3$ and Fig. 4(e) with $\mu = 0.8$. In the two sub-figures, the blue closed lines are Fermi surfaces $E(k_x, k_y, k_z)$, and the red lines are their particle-hole counterparts $E(-k_x, -k_y, \pi - k_z)$ considering the pairing momentum $2\mathbf{Q}$. As shown in Fig. 4(e), for a greater μ , there could be significant difference between $E(k_x, k_y, k_z)$ and $-E(k_x, -k_y, \pi - k_z)$, which will hinder the pairing with momentum $2\mathbf{Q}$. On the other hand,

because there is inversion symmetry in this model, we have $E(k_x, k_y, k_z) = E(-k_x, -k_y, -k_z)$. So the Fermi surfaces and their particle-hole counterparts considering zero momentum pairing always overlap, and the pairing with momentum $\mathbf{0}$ will not be weakened. Thus, increasing the chemical potential will suppress the FF phase with pairing momentum $2\mathbf{Q}$, and the BCS pairing with momentum $\mathbf{0}$ will dominate, corresponding to the BCS phase (the red region). Second, we find that if U is large enough, the FF pairing always dominates. Let's explain this by using the information given in Fig. 4(f), where the spin textures are plotted on the Fermi surfaces. Because we are considering the singlet pairing, the pairing between electrons with opposite spins will be favored. As shown in Fig. 4(f), the spin of the electron at (k_x, k_y, k_z) is almost opposite to that of the electron at $(-k_x, -k_y, \pi - k_z)$ for every point on the Fermi surfaces. However, only a small portion of the electrons on the Fermi surfaces satisfy the condition that the spin of the electron at (k_x, k_y, k_z) is opposite to that of the electron at $(-k_x, -k_y, -k_z)$. As a result, the FF pairing between two electrons with total momentum $2\mathbf{Q}$ is favored. Although in the BCS phase (the red region) the FF pairing is suppressed due to the off-resonance between particle and hole bands, if U is large enough, the interaction will compensate for such energy difference. In this case, the role of spin textures become dominant, and FF pairing will be favored, which corresponds to the FF phase (the purple region) in Fig. 4(f).

The phase diagram Fig. 4(b) is obtained by assuming the order parameters Δ_0 and $\Delta_{2\mathbf{Q}}$ are real. Seriously speaking, such assumption is too strong. In fact, there could be a phase differences between the two order parameters. However, if we solve the self-consistent gap equations with a phase difference between the two order parameters, we find that the main features of the phase diagram in the above paragraph are preserved. For example, the self-consistent solution for the parameter $\mu = 0.8$ and $U = 7$ in the phase diagram Fig. 4(b) are $\Delta_0 = 0.592$ and $\Delta_{2\mathbf{Q}} = 0$. After considering the phase difference between the two parameters, the self-consistent solutions are still $|\Delta_0| = 0.592$ and $|\Delta_{2\mathbf{Q}}| = 0$. We also find that for the points around $\mu = 0.8$ and $U = 7$, we still obtain BCS phase. Thus, the BCS phase in the phase diagram Fig. 4(b) are still reliable even if we consider the phase difference between the two parameters.

VI. THE k_z -DEPENDENT CHERN-SIMONS TERM

In this section we will propose the topological invariants characterizing the aforementioned MFBs in the vortex line of SC Weyl semimetals. Because the vortex line along z direction preserves the translation symmetry in z direction, k_z is a good quantum number. For this reason, we decompose the VBs of SC Weyl semimetals into the VBs of SC Chern insulators labelled by k_z . Similarly,

the topological invariants characterizing the VBSs are also defined for each k_z .

When k_z is fixed, we obtain a 2D SC Chern insulator belonging to class D, and the vortex line becomes a point defect. According to the classification of topological defects [79], for a point defect in 2D, the Hamiltonian will depend on 2 momentum variables and 1 position variable. In this case, the parameters in \mathbf{k} space k_x, k_y , and the real space parameter ϕ make up the three dimensional synthetic space $T^2 \times S^1$, where ϕ is the polar angle in the real 2D space. It is shown that a point defect in class D is characterized by a Z_2 invariant determining the presence or absence of Majorana zero modes [29, 79]. The Z_2 invariant is the so-called Chern-Simons invariant

$$\nu = \frac{2}{2!} \left(\frac{i}{2\pi} \right)^2 \int_{T^2 \times S^1} \mathcal{Q}_3 \pmod{2}. \quad (8)$$

Here \mathcal{Q}_3 is the Chern-Simon form

$$\mathcal{Q}_3 = \text{Tr}[AdA + \frac{2}{3}A^3], \quad (9)$$

where \mathcal{A} is the Berry's connection.

For a 2D SC Chern insulators (obtained at k_z in the SC Weyl semimetal) with BdG Chern number $C(k_z)$ and a vortex with vorticity n , it is shown that the Z_2 invariant characterizing the vortex mode is [29, 79]

$$v(k_z) = C(k_z)n \pmod{2}. \quad (10)$$

Throughout this article, we consider the vortex with $n = 1$, thus Eq. (10) reduces to $\nu = C(k_z) \pmod{2}$. That is, if the BdG Chern number $C(k_z)$ of the SC Chern insulator obtained at k_z in the SC Weyl semimetal is odd, there will be Majorana zero modes in the vortex core, which is consistent with the arguments we use to explore the appearance of MFBs in the previous texts. Thus, the k_z -dependent Chern-Simon invariant Eq. (10) is the expected topological invariant for characterizing the MFBs in the vortex line of SC Weyl semimetals.

VII. SUMMARY AND DISCUSSIONS

In summary, we have calculated the VBSs of SC Weyl semimetals which breaks time reversal symmetry and obtain the MFBs in the vortex line. To understand the appearance of the MFBs, we first show that the Weyl semimetal can be decomposed into stacked Chern insulators with different Chern numbers. Then we calculate the topological phase diagram of the corresponding SC Chern insulators through both analytical and numerical methods. By mapping the SC Weyl semimetal into a series of SC Chern insulators, we understand the MFBs as the Majorana zero modes in the vortex line of SC Chern insulators with odd BdG Chern numbers. To realize the SC Weyl semimetal with BCS pairing, we consider the Weyl semimetal with attractive Hubbard interaction. We find that under appropriate parameters, the mean field

calculations will give the SC Weyl semimetal in BCS phase. Finally, based on the previous study about the classification of topological defects, we propose the k_z -dependent Z_2 Chern-Simons invariant to characterize the MFBs.

It is worthwhile to point out that different from Weyl semimetals breaking time reversal symmetry, the VBSs of time reversal symmetric Weyl semimetals can host propagating gapless Majorana modes [63]. This is because the low-energy effective BdG Hamiltonian of a SC time reversal symmetric Weyl semimetal consists of mutually anti-commuting matrices, and the spectra are fully gapped, and the in-gap gapless Majorana modes are protected by the emergent second Chern number. In our case, things are quite different. The spectra of the effective BdG Hamiltonian of a SC time reversal symmetric Weyl semimetal is gapless, and we cannot define the second Chern number to protect a propagating gapless Majorana modes. Instead, we can study the VBSs for each k_z , and Majorana zero modes in a certain range of k_z constitute the MFBs.

ACKNOWLEDGMENTS

We appreciate the valuable discussions with Dr. Ting Fung Jeffrey Poon about the calculations of Chern numbers and the mean-field method considering the folded Brillouin zone. We also thank Professor X.J. Liu, S.S. Qin, and J.S. Hong for helpful discussions.

Appendix A: The Mean Field Approach

The pairing term in the BdG Hamiltonian Eq. (3) is added by hand, which lacks a clear origin. Now we give a model considering the attractive Hubbard interaction, and the ground state calculated by the mean field approach can be BCS pairing state under appropriate parameters.

1. The Model and the Mean Field Approximation

The model considering the attractive Hubbard interaction reads

$$H_{\text{int}} = \sum_{\mathbf{k}} \psi^\dagger(\mathbf{k})(H_{\text{WSM}}(\mathbf{k}) - \mu)\psi(\mathbf{k}) - U \sum_i n_{i\uparrow}n_{i\downarrow}, \quad (A1)$$

where $\psi(\mathbf{k}) = (c_{\mathbf{k},\uparrow}, c_{\mathbf{k},\downarrow})^T$. We may perform the Fourier transform on the attractive Hubbard interaction term and obtain

$$H_{\text{int}} = \sum_{\mathbf{k}} \psi^\dagger(\mathbf{k})(H_{\text{WSM}}(\mathbf{k}) - \mu)\psi(\mathbf{k}) - \frac{U}{V} \sum_{\mathbf{q}} \sum_{\mathbf{k}} \sum_{\mathbf{k}'} c_{\mathbf{k}'+\mathbf{q},\uparrow}^\dagger c_{-\mathbf{k}',\downarrow}^\dagger c_{-\mathbf{k},\downarrow} c_{\mathbf{k}+\mathbf{q},\uparrow}. \quad (A2)$$

As depicted in Fig. 4, the Fermi surface for $\mu \neq 0$ consists of two closed circles around the two Weyl points. Thus, it is reasonable to consider the pairing with momentum $\mathbf{q} = \mathbf{0}$ or $\mathbf{q} = 2\mathbf{Q}$ ($\mathbf{Q} = (0, 0, \pi/2)$). Then we keep only two terms with $\mathbf{q} = \mathbf{0}$ and $\mathbf{q} = 2\mathbf{Q}$ in the summation of \mathbf{q} in Eq. (A2).

$$\begin{aligned} H_{\text{int}} &= \sum_{\mathbf{k}} \psi^\dagger(\mathbf{k})(H_{\text{WSM}}(\mathbf{k}) - \mu)\psi(\mathbf{k}) \\ &\quad - \frac{U}{V} \sum_{\mathbf{k}} \sum_{\mathbf{k}'} c_{\mathbf{k}',\uparrow}^\dagger c_{-\mathbf{k}',\downarrow}^\dagger c_{-\mathbf{k},\downarrow} c_{\mathbf{k},\uparrow} \\ &\quad - \frac{U}{V} \sum_{\mathbf{k}} \sum_{\mathbf{k}'} c_{\mathbf{k}',\uparrow}^\dagger c_{-\mathbf{k}',\downarrow}^\dagger c_{-\mathbf{k},\downarrow} c_{\mathbf{k}+2\mathbf{Q},\uparrow}. \end{aligned} \quad (\text{A3})$$

Next we apply the mean field approximation and define the order parameter $\Delta_{\mathbf{q}} = -\frac{U}{V} \sum_{\mathbf{k}} \langle c_{-\mathbf{k},\downarrow} c_{\mathbf{k}+\mathbf{q},\uparrow} \rangle$. Correspondingly, the interaction term can be approximated as

$$\begin{aligned} & - \frac{U}{V} \sum_{\mathbf{k}} \sum_{\mathbf{k}'} c_{\mathbf{k}'+\mathbf{q},\uparrow}^\dagger c_{-\mathbf{k}',\downarrow}^\dagger c_{-\mathbf{k},\downarrow} c_{\mathbf{k}+\mathbf{q},\uparrow} \\ & \approx \sum_{\mathbf{k}} \Delta_{\mathbf{q}}^* c_{-\mathbf{k},\downarrow} c_{\mathbf{k}+\mathbf{q},\uparrow} + \sum_{\mathbf{k}} \Delta_{\mathbf{q}} c_{\mathbf{k}+\mathbf{q},\uparrow}^\dagger c_{-\mathbf{k},\downarrow}^\dagger + \frac{V}{U} |\Delta_{\mathbf{q}}|^2. \end{aligned} \quad (\text{A4})$$

Substituting the mean field approximation Eq. (A4) into Eq. (A3), we obtain the following result.

$$\begin{aligned} H_{\text{int}} &= \sum_{\mathbf{k}} \psi^\dagger(\mathbf{k})(H_{\text{WSM}}(\mathbf{k}) - \mu)\psi(\mathbf{k}) \\ &+ \sum_{\mathbf{k}} \Delta_0^* c_{-\mathbf{k},\downarrow} c_{\mathbf{k},\uparrow} + \sum_{\mathbf{k}} \Delta_0 c_{\mathbf{k},\uparrow}^\dagger c_{-\mathbf{k},\downarrow}^\dagger + \frac{V}{U} |\Delta_0|^2 \\ &+ \sum_{\mathbf{k}} \Delta_{2\mathbf{Q}}^* c_{-\mathbf{k},\downarrow} c_{\mathbf{k}+2\mathbf{Q},\uparrow} + \sum_{\mathbf{k}} \Delta_{2\mathbf{Q}} c_{\mathbf{k}+2\mathbf{Q},\uparrow}^\dagger c_{-\mathbf{k},\downarrow}^\dagger + \frac{V}{U} |\Delta_{2\mathbf{Q}}|^2. \end{aligned} \quad (\text{A5})$$

To express the above model in the form of a BdG Hamiltonian, we rewrite each term in it. First we deal with the normal state Hamiltonian of the Weyl semimetal.

$$\begin{aligned} & \sum_{\mathbf{k}} \psi^\dagger(\mathbf{k})(H_{\text{WSM}}(\mathbf{k}) - \mu)\psi(\mathbf{k}) \\ &= \frac{1}{2} \left\{ \sum_{\mathbf{k}} \psi^\dagger(\mathbf{k}) H_N(\mathbf{k}) \psi(\mathbf{k}) + \sum_{\mathbf{k}} \psi^\dagger(\mathbf{k}) H_N(\mathbf{k}) \psi(\mathbf{k}) \right\} \\ &= \frac{1}{2} \sum_{\mathbf{k}} \psi^\dagger(\mathbf{k}) H_N(\mathbf{k}) \psi(\mathbf{k}) + \frac{1}{2} \sum_{\mathbf{k}} \text{Tr} H_N(\mathbf{k}) \\ &+ \frac{1}{2} \sum_{\mathbf{k}} -\psi^T(-\mathbf{k}) H_N^*(-\mathbf{k}) (\psi^\dagger(-\mathbf{k}))^T. \end{aligned} \quad (\text{A6})$$

Here we have used the notation $H_N(\mathbf{k}) = H_{\text{WSM}}(\mathbf{k}) - \mu$. Then the pairing terms are rewritten in the following

form.

$$\begin{aligned} & \sum_{\mathbf{k}} \Delta_{\mathbf{q}}^* c_{-\mathbf{k},\downarrow} c_{\mathbf{k}+\mathbf{q},\uparrow} + \sum_{\mathbf{k}} \Delta_{\mathbf{q}} c_{\mathbf{k}+\mathbf{q},\uparrow}^\dagger c_{-\mathbf{k},\downarrow}^\dagger \\ &= \frac{1}{2} \sum_{\mathbf{k}} \Delta_{\mathbf{q}}^* c_{-\mathbf{k},\downarrow} c_{\mathbf{k}+\mathbf{q},\uparrow} + \frac{1}{2} \sum_{\mathbf{k}} \Delta_{\mathbf{q}} c_{\mathbf{k}+\mathbf{q},\uparrow}^\dagger c_{-\mathbf{k},\downarrow}^\dagger \\ &\quad - \frac{1}{2} \sum_{\mathbf{k}} \Delta_{\mathbf{q}}^* c_{-\mathbf{k},\uparrow} c_{\mathbf{k}+\mathbf{q},\downarrow} - \frac{1}{2} \sum_{\mathbf{k}} \Delta_{\mathbf{q}} c_{\mathbf{k}+\mathbf{q},\downarrow}^\dagger c_{-\mathbf{k},\uparrow}^\dagger. \end{aligned} \quad (\text{A7})$$

Obviously, as mentioned above, we only need consider $\mathbf{q} = \mathbf{0}$ and $\mathbf{q} = 2\mathbf{Q}$ cases.

2. The Brillouin Zone Folding and the Self-consistent Equations

Because the two pairing terms with momenta $\mathbf{q} = \mathbf{0}$ and $\mathbf{q} = 2\mathbf{Q}$ coexist in the Hamiltonian Eq. (A5), we cannot write it in the form of a BdG Hamiltonian under the basis $\Psi^\dagger(\mathbf{k}) = (c_{\mathbf{k},\uparrow}^\dagger, c_{\mathbf{k},\downarrow}^\dagger, c_{-\mathbf{k},\uparrow}, c_{-\mathbf{k},\downarrow})$ with k_x, k_y , and k_z in the range $(-\pi, \pi]$. Instead, we have to consider the folded Brillouin zone (FBZ) with $k_x, k_y \in (-\pi, \pi]$ and $k_z \in (0, \pi]$, corresponding to the pairing momentum $2\mathbf{Q} = (0, 0, \pi)$. Now the normal state Hamiltonian can be written as

$$\begin{aligned} & \sum_{\mathbf{k}} \psi^\dagger(\mathbf{k}) H_N(\mathbf{k}) \psi(\mathbf{k}) \\ &= \sum_{\mathbf{k} \in \text{FBZ}} \psi^\dagger(\mathbf{k}) H_N(\mathbf{k}) \psi(\mathbf{k}) \\ &\quad + \sum_{\mathbf{k} \in \text{FBZ}} \psi^\dagger(\mathbf{k} + 2\mathbf{Q}) H_N(\mathbf{k} + 2\mathbf{Q}) \psi(\mathbf{k} + 2\mathbf{Q}). \end{aligned} \quad (\text{A8})$$

Similarly, the pairing terms can also be written in the FBZ. Corresponding to the FBZ, the new basis becomes $\Psi^\dagger(\mathbf{k}) = (\tilde{c}_{\mathbf{k}}^\dagger, \tilde{c}_{\mathbf{k}+2\mathbf{Q}}^\dagger, \tilde{c}_{-\mathbf{k}}, \tilde{c}_{-\mathbf{k}-2\mathbf{Q}})$, where we have defined $\tilde{c}_{\mathbf{k}}^\dagger = (c_{\mathbf{k},\uparrow}^\dagger, c_{\mathbf{k},\downarrow}^\dagger)$. Under the new basis considering the FBZ, the Hamiltonian now takes the following form

$$\begin{aligned} H &= \frac{V}{U} |\Delta_0|^2 + \frac{V}{U} |\Delta_{2\mathbf{Q}}|^2 + \frac{1}{2} \sum_{\mathbf{k}} \text{Tr} H_N(\mathbf{k}) \\ &\quad + \frac{1}{2} \sum_{\mathbf{k} \in \text{FBZ}} \Psi^\dagger(\mathbf{k}) H_{\text{BdG}}(\mathbf{k}) \Psi(\mathbf{k}), \end{aligned} \quad (\text{A9})$$

where the explicit form of $H_{\text{BdG}}(\mathbf{k})$ is

$$\begin{pmatrix} H_N(\mathbf{k}) & \mathbf{0}_{2 \times 2} & \tilde{\Delta}_0 & \tilde{\Delta}_{2\mathbf{Q}} \\ \mathbf{0}_{2 \times 2} & H_N(\mathbf{k} + 2\mathbf{Q}) & \tilde{\Delta}_{2\mathbf{Q}} & \tilde{\Delta}_0 \\ \tilde{\Delta}_0^\dagger & \tilde{\Delta}_{2\mathbf{Q}}^\dagger & -H_N^*(-\mathbf{k}) & \mathbf{0}_{2 \times 2} \\ \tilde{\Delta}_{2\mathbf{Q}}^\dagger & \tilde{\Delta}_0^\dagger & \mathbf{0}_{2 \times 2} & -H_N^*(-\mathbf{k} - 2\mathbf{Q}) \end{pmatrix}. \quad (\text{A10})$$

Here we have used the notation

$$\tilde{\Delta}_{\mathbf{q}} = \begin{pmatrix} 0 & \Delta_{\mathbf{q}} \\ -\Delta_{\mathbf{q}} & 0 \end{pmatrix}. \quad (\text{A11})$$

Suppose that we can diagonalize the BdG Hamiltonian in the following way

$$\begin{aligned}
& \frac{1}{2} \sum_{\mathbf{k} \in \text{FBZ}} \Psi^\dagger(\mathbf{k}) H_{\text{BdG}}(\mathbf{k}) \Psi(\mathbf{k}) \\
&= \frac{1}{2} \sum_{\mathbf{k} \in \text{FBZ}} \Psi^\dagger(\mathbf{k}) U(\mathbf{k}) U^{-1}(\mathbf{k}) H_{\text{BdG}}(\mathbf{k}) U(\mathbf{k}) U^{-1}(\mathbf{k}) \Psi(\mathbf{k}) \\
&= \frac{1}{2} \sum_{\mathbf{k} \in \text{FBZ}} \sum_{i=1}^8 E_i(\mathbf{k}) \Gamma_i^\dagger(\mathbf{k}) \Gamma_i(\mathbf{k}),
\end{aligned} \tag{A12}$$

in which the unitary matrix $U(\mathbf{k})$ diagonalizes $H_{\text{BdG}}(\mathbf{k})$, and we define $\Gamma(\mathbf{k}) \equiv U^{-1}(\mathbf{k})$. According to the definition of the order parameter $\Delta_{2\mathbf{Q}} = -\frac{U}{V} \sum_{\mathbf{k}} \langle c_{-\mathbf{k}, \downarrow} c_{\mathbf{k}+2\mathbf{Q}, \uparrow} \rangle$, we obtain the self-consistent equation

$$\begin{aligned}
\Delta_{2\mathbf{Q}} &= -\frac{U}{V} \sum_{\mathbf{k}} \langle c_{-\mathbf{k}, \downarrow} c_{\mathbf{k}+2\mathbf{Q}, \uparrow} \rangle \\
&= -\frac{U}{V} \sum_{\mathbf{k} \in \text{FBZ}} \langle c_{-\mathbf{k}, \downarrow} c_{\mathbf{k}+2\mathbf{Q}, \uparrow} \rangle - \frac{U}{V} \sum_{\mathbf{k} \in \text{FBZ}} \langle c_{-\mathbf{k}-2\mathbf{Q}, \downarrow} c_{\mathbf{k}, \uparrow} \rangle \\
&= -\frac{U}{V} \sum_{\mathbf{k} \in \text{FBZ}} \langle \Gamma_n^\dagger U_{n6}^{-1} U_{3m} \Gamma_m \rangle - \frac{U}{V} \sum_{\mathbf{k} \in \text{FBZ}} \langle \Gamma_n^\dagger U_{n8}^{-1} U_{1m} \Gamma_m \rangle \\
&= -\frac{U}{V} \sum_{\mathbf{k} \in \text{FBZ}} \delta_{mn} f(E_{\mathbf{k}}^n) U_{n6}^{-1} U_{3m} - \delta_{mn} f(E_{\mathbf{k}}^n) U_{n8}^{-1} U_{1m}.
\end{aligned} \tag{A13}$$

Similarly, we can obtain the self-consistent equation of the order parameter Δ_0

$$\begin{aligned}
\Delta_0 &= -\frac{U}{V} \sum_{\mathbf{k} \in \text{FBZ}} \delta_{mn} f(E_{\mathbf{k}}^n) U_{n6}^{-1} U_{1m} \\
&\quad - \frac{U}{V} \sum_{\mathbf{k} \in \text{FBZ}} \delta_{mn} f(E_{\mathbf{k}}^n) U_{n8}^{-1} U_{3m}.
\end{aligned} \tag{A14}$$

In principle, we can obtain the order parameters Δ_0 and $\Delta_{2\mathbf{Q}}$ by solving the two self-consistent equations (A13) and (A14).

3. The Free Energy

The definition of free energy is $\Omega = -\frac{1}{\beta} \log Z$, where Z is the partition function of the system we study. According to the knowledge in quantum statistics, we can calculate the partition function through the following formula

$$Z = \text{Tr} e^{-\beta H} = e^{-\beta \text{Const.}} \text{Tr} e^{-\beta \frac{1}{2} \sum_{\mathbf{k} \in \text{FBZ}} \sum_{i=1}^8 E_i(\mathbf{k}) \Gamma_i^\dagger(\mathbf{k}) \Gamma_i(\mathbf{k})}. \tag{A15}$$

Here $\text{Const.} = \frac{V}{U} |\Delta_0|^2 + \frac{V}{U} |\Delta_{2\mathbf{Q}}|^2 + \frac{1}{2} \sum_{\mathbf{k}} \text{Tr} H_N(\mathbf{k})$. We can readily evaluate the partition function [80], because after diagonalizing the BdG Hamiltonian, we obtain a system consists of free fermions. Then we obtain the free

energy

$$\begin{aligned}
\Omega &= -\frac{1}{\beta} \log e^{-\beta \text{Const.}} \\
&\quad - \frac{1}{2\beta} \log \prod_{\mathbf{k} \in \text{FBZ}} (1 + e^{-\beta E_{\mathbf{k}}^1}) \cdots (1 + e^{-\beta E_{\mathbf{k}}^8}) \\
&= \frac{V}{U} |\Delta_0|^2 + \frac{V}{U} |\Delta_{2\mathbf{Q}}|^2 + \frac{1}{2} \sum_{\mathbf{k}} \text{Tr} H_N(\mathbf{k}) \\
&\quad - \frac{1}{2\beta} \sum_{\mathbf{k} \in \text{FBZ}} \log(1 + e^{-\beta E_{\mathbf{k}}^1}) + \cdots + \log(1 + e^{-\beta E_{\mathbf{k}}^8}).
\end{aligned} \tag{A16}$$

Since we may obtain the self-consistent solutions around the local minima of the free energy, we can compare the free energy of solutions around different local minima to obtain the self-consistent solutions at the global minimum of the free energy. On the other hand, it is well known that the solutions of the self-consistent equations satisfying $\frac{\partial \Omega}{\partial \Delta} = 0$. Thus, we may plot the $\Omega - \Delta$ relation to check whether we have solve the self-consistent equations correctly. Here is an example. As shown in Fig. 5(a), when we set the parameters as $\mu = 0.6$ and $U = 7$, the

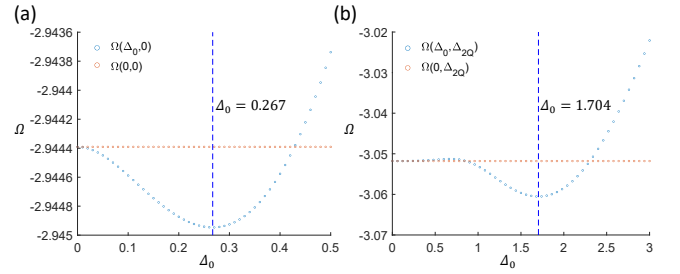


FIG. 5. (a) The $\Omega - \Delta_0$ relation with $\Delta_{2\mathbf{Q}} = 0$. The parameters are set as $\mu = 0.6$ and $U = 7$. (b) The $\Omega - \Delta_0$ relation with $\Delta_{2\mathbf{Q}} = 0.741$. The parameters take the values $\mu = 0.7$ and $U = 8$.

self-consistent equations give the solutions $\Delta_0 = 0.267$ and $\Delta_{2\mathbf{Q}} = 0$, which is the BCS phase. On the other hand, since we have obtained the explicit expression for the free energy, we can plot the $\Omega - \Delta_0$ relation with $\Delta_{2\mathbf{Q}} = 0$. It is easy to find that the solution of the self-consistent equations $\Delta_0 = 0.267$ minimizes the free energy. When the parameters take the values $\mu = 0.7$ and $U = 8$, the solutions of the self-consistent equations are $\Delta_0 = 1.704$ and $\Delta_{2\mathbf{Q}} = 0.741$, corresponding to the coexistence of BCS phase and FF phase. Fig. 5(b) shows the $\Omega - \Delta_0$ relation with $\Delta_{2\mathbf{Q}} = 0.741$. Obviously, the solution $\Delta_0 = 1.704$ minimizes the free energy, verifying our self-consistent calculations.

Appendix B: The Finite Size Effect around the Boundaries of the MFBS

In the main text, we notice that although the real boundaries of the MFBS are relatively close to the exact

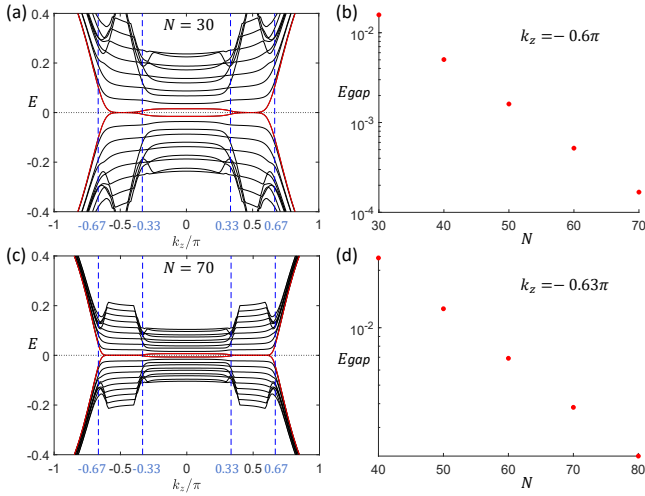


FIG. 6. (a) and (c) show the VBSs of SC Weyl semimetals with $\mu = 0$ and $\Delta = 0.5$. The lattice sizes in (a) and (c) are $N = 30$ and $N = 70$, respectively. (b) and (d) show how the gap of the VBSs change as we increase the lattice size. (b) is calculated at $k_z = -0.6\pi$, and (d) is calculated at $k_z = -0.63\pi$. Both (b) and (d) are calculated with the parameters $\mu = 0$ and $\Delta = 0.5$.

boundaries given by the topological phase diagram, there is notable difference between them. In this section, we

will illustrate that such discrepancy is due to the finite size effect, and the real boundaries of the MFBs will approach the exact boundaries given by the topological phase diagram.

To be specific, we focus the $\mu = 0$ and $\Delta = 0.5$ case. Fig. 6(a) and Fig. 6(c) show the VBSs of SC Weyl semimetals with lattice size $N = 30$ and $N = 70$, respectively. Obviously, compared to the real boundaries of the MFBs in $N = 30$ case, as we increase the lattice size to $N = 70$, the real boundaries of the MFBs are much more close to the exact phase boundaries (the blue dashed line). Correspondingly, we notice that the MFBs occupy more space on the k_z axis, but they are still constrained within the regions enclosed by the exact boundaries (the blue dashed lines).

We can also analyze the finite size effect by observing the behavior of the gap in the VBSs at a fixed k_z as we increase the lattice size. As shown in Fig. 4(b), we fix $k_z = -0.6\pi$ and increase the lattice to calculate the VBSs. We find that the gap of the VBSs at $k_z = -0.6\pi$ decreases exponentially as the lattice size N increases. A similar result appear in Fig. 6(d), in which the gap also decreases exponentially as we increase N . Thus, we attribute the discrepancy between the real boundaries of MFBs and the exact boundaries obtained from the topological phase diagrams to the finite size effect. Based on the results in Fig. 6, it is natural to expect that when the lattice size is large enough, the boundaries of the MFBs will be the exact phase boundaries.

-
- [1] L. Fu and C. L. Kane, *Phys. Rev. Lett.* **100**, 096407 (2008).
- [2] M. Z. Hasan and C. L. Kane, *Rev. Mod. Phys.* **82**, 3045 (2010).
- [3] X.-L. Qi and S.-C. Zhang, *Rev. Mod. Phys.* **83**, 1057 (2011).
- [4] J. Alicea, Reports on progress in physics **75**, 076501 (2012).
- [5] H. Zhang, C.-X. Liu, X.-L. Qi, X. Dai, Z. Fang, and S.-C. Zhang, *Nature physics* **5**, 438 (2009).
- [6] L. Fu and E. Berg, *Phys. Rev. Lett.* **105**, 097001 (2010).
- [7] C.-K. Chiu, M. J. Gilbert, and T. L. Hughes, *Phys. Rev. B* **84**, 144507 (2011).
- [8] C.-K. Chiu, P. Ghaemi, and T. L. Hughes, *Phys. Rev. Lett.* **109**, 237009 (2012).
- [9] Y. S. Hor, J. G. Checkelsky, D. Qu, N. Ong, and R. J. Cava, *Journal of Physics and Chemistry of Solids* **72**, 572 (2011).
- [10] J. Zhang, S. Zhang, H. Weng, W. Zhang, L. Yang, Q. Liu, S. Feng, X. Wang, R. Yu, L. Cao, *et al.*, *Proceedings of the National Academy of Sciences* **108**, 24 (2011).
- [11] P. Hosur, P. Ghaemi, R. S. K. Mong, and A. Vishwanath, *Phys. Rev. Lett.* **107**, 097001 (2011).
- [12] J.-P. Xu, M.-X. Wang, Z. L. Liu, J.-F. Ge, X. Yang, C. Liu, Z. A. Xu, D. Guan, C. L. Gao, D. Qian, Y. Liu, Q.-H. Wang, F.-C. Zhang, Q.-K. Xue, and J.-F. Jia, *Phys. Rev. Lett.* **114**, 017001 (2015).
- [13] H.-H. Sun, K.-W. Zhang, L.-H. Hu, C. Li, G.-Y. Wang, H.-Y. Ma, Z.-A. Xu, C.-L. Gao, D.-D. Guan, Y.-Y. Li, C. Liu, D. Qian, Y. Zhou, L. Fu, S.-C. Li, F.-C. Zhang, and J.-F. Jia, *Phys. Rev. Lett.* **116**, 257003 (2016).
- [14] S. A. A. Ghorashi, T. L. Hughes, and E. Rossi, *Phys. Rev. Lett.* **125**, 037001 (2020).
- [15] R.-X. Zhang, (2022), [arXiv:2208.01652](https://arxiv.org/abs/2208.01652).
- [16] L.-H. Hu and R.-X. Zhang, *Nature Communications* **14**, 640 (2023).
- [17] S. M. Young, S. Zaheer, J. C. Y. Teo, C. L. Kane, E. J. Mele, and A. M. Rappe, *Phys. Rev. Lett.* **108**, 140405 (2012).
- [18] B.-J. Yang and N. Nagaosa, *Nature Communications* **5**, 4898 (2014).
- [19] Z. Wang, H. Weng, Q. Wu, X. Dai, and Z. Fang, *Phys. Rev. B* **88**, 125427 (2013).
- [20] Z. Wang, Y. Sun, X.-Q. Chen, C. Franchini, G. Xu, H. Weng, X. Dai, and Z. Fang, *Phys. Rev. B* **85**, 195320 (2012).
- [21] Z. Liu, J. Jiang, B. Zhou, Z. Wang, Y. Zhang, H. Weng, D. Prabhakaran, S. K. Mo, H. Peng, P. Dudin, *et al.*, *Nature materials* **13**, 677 (2014).
- [22] L. He, Y. Jia, S. Zhang, X. Hong, C. Jin, and S. Li, *npj Quantum Materials* **1**, 1 (2016).
- [23] J. Song, S. Kim, Y. Kim, H. Fu, J. Koo, Z. Wang, G. Lee, J. Lee, S. H. Oh, J. Bang, T. Matsushita, N. Wada, H. Ikegami, J. D. Denlinger, Y. H. Lee, B. Yan, Y. Kim, and S. W. Kim, *Phys. Rev. X* **11**, 021065 (2021).
- [24] Y. Zhou, B. Li, Z. Lou, H. Chen, Q. Chen, B. Xu, C. Wu,

- J. Du, J. Yang, H. Wang, *et al.*, *Science China Physics, Mechanics & Astronomy* **64**, 247411 (2021).
- [25] X. P. Yang, Y. Zhong, S. Mardanya, T. A. Cochran, R. Chapai, A. Mine, J. Zhang, J. Sánchez-Barriga, Z.-J. Cheng, O. J. Clark, J.-X. Yin, J. Blawat, G. Cheng, I. Belopolski, T. Nagashima, S. Najafzadeh, S. Gao, N. Yao, A. Bansil, R. Jin, T.-R. Chang, S. Shin, K. Okazaki, and M. Z. Hasan, *Phys. Rev. Lett.* **130**, 046402 (2023).
- [26] M. Kheirkhah, Z.-Y. Zhuang, J. Maciejko, and Z. Yan, *Phys. Rev. B* **105**, 014509 (2022).
- [27] S. Qin, L. Hu, C. Le, J. Zeng, F.-c. Zhang, C. Fang, and J. Hu, *Phys. Rev. Lett.* **123**, 027003 (2019).
- [28] Z. Yan, Z. Wu, and W. Huang, *Phys. Rev. Lett.* **124**, 257001 (2020).
- [29] C. Chan, L. Zhang, T. F. J. Poon, Y.-P. He, Y.-Q. Wang, and X.-J. Liu, *Phys. Rev. Lett.* **119**, 047001 (2017).
- [30] S. Kobayashi and M. Sato, *Phys. Rev. Lett.* **115**, 187001 (2015).
- [31] F. Fei, X. Bo, P. Wang, J. Ying, J. Li, K. Chen, Q. Dai, B. Chen, Z. Sun, M. Zhang, *et al.*, *Advanced Materials* **30**, 1801556 (2018).
- [32] S. Kobayashi, S. Sumita, M. Hirayama, and A. Furusaki, *Physical Review B* **107**, 214518 (2023).
- [33] A. T. Lee, K. Park, and I.-H. Lee, *Phys. Rev. B* **107**, 115127 (2023).
- [34] G. Xu, B. Lian, P. Tang, X.-L. Qi, and S.-C. Zhang, *Phys. Rev. Lett.* **117**, 047001 (2016).
- [35] Z. Wang, P. Zhang, G. Xu, L. K. Zeng, H. Miao, X. Xu, T. Qian, H. Weng, P. Richard, A. V. Fedorov, H. Ding, X. Dai, and Z. Fang, *Phys. Rev. B* **92**, 115119 (2015).
- [36] X. Wu, S. Qin, Y. Liang, H. Fan, and J. Hu, *Phys. Rev. B* **93**, 115129 (2016).
- [37] S. Qin, L. Hu, X. Wu, X. Dai, C. Fang, F.-C. Zhang, and J. Hu, *Science Bulletin* **64**, 1207 (2019).
- [38] L.-H. Hu, X. Wu, C.-X. Liu, and R.-X. Zhang, *Phys. Rev. Lett.* **129**, 277001 (2022).
- [39] M. Kheirkhah, Z. Yan, and F. Marsiglio, *Phys. Rev. B* **103**, L140502 (2021).
- [40] D. Wang, L. Kong, P. Fan, H. Chen, S. Zhu, W. Liu, L. Cao, Y. Sun, S. Du, J. Schneeloch, *et al.*, *Science* **362**, 333 (2018).
- [41] P. Zhang, K. Yaji, T. Hashimoto, Y. Ota, T. Kondo, K. Okazaki, Z. Wang, J. Wen, G. Gu, H. Ding, *et al.*, *Science* **360**, 182 (2018).
- [42] L. Kong, S. Zhu, M. Papaj, H. Chen, L. Cao, H. Isobe, Y. Xing, W. Liu, D. Wang, P. Fan, *et al.*, *Nature Physics* **15**, 1181 (2019).
- [43] A. Ghazaryan, P. L. S. Lopes, P. Hosur, M. J. Gilbert, and P. Ghaemi, *Phys. Rev. B* **101**, 020504 (2020).
- [44] E. J. König and P. Coleman, *Phys. Rev. Lett.* **122**, 207001 (2019).
- [45] A. A. Burkov and L. Balents, *Phys. Rev. Lett.* **107**, 127205 (2011).
- [46] G. Xu, H. Weng, Z. Wang, X. Dai, and Z. Fang, *Phys. Rev. Lett.* **107**, 186806 (2011).
- [47] X. Wan, A. M. Turner, A. Vishwanath, and S. Y. Savrasov, *Phys. Rev. B* **83**, 205101 (2011).
- [48] A. Nomani and P. Hosur, Intrinsic surface superconducting instability in type-i weyl semimetals (2023), [arXiv:2304.02635 \[cond-mat.str-el\]](https://arxiv.org/abs/2304.02635).
- [49] W. Deng, J. Zhen, Q. Huang, Y. Wang, H. Dong, S. Wan, S. Zhang, J. Feng, and B. Chen, *The Journal of Physical Chemistry Letters* **13**, 5514 (2022).
- [50] A. Kononov, M. Endres, G. Abulizi, K. Qu, J. Yan, D. G. Mandrus, K. Watanabe, T. Taniguchi, and C. Schönberger, *Journal of Applied Physics* **129**, 113903 (2021).
- [51] W. Cao, N. Zhao, C. Pei, Q. Wang, Q. Zhang, T. Ying, Y. Zhao, L. Gao, C. Li, N. Yu, L. Gu, Y. Chen, K. Liu, and Y. Qi, *Phys. Rev. B* **105**, 174502 (2022).
- [52] X.-H. Tu, T. Bo, P.-F. Liu, W. Yin, N. Hao, and B.-T. Wang, *Physical Chemistry Chemical Physics* **24**, 7893 (2022).
- [53] Q.-G. Mu, D. Nenno, Y.-P. Qi, F.-R. Fan, C. Pei, M. ElGhazali, J. Gooth, C. Felser, P. Narang, and S. Medvedev, *Phys. Rev. Mater.* **5**, 084201 (2021).
- [54] M. R. Van Delft, S. Pezzini, M. König, P. Tinnemans, N. E. Hussey, and S. Wiedmann, *Crystals* **10**, 288 (2020).
- [55] H. Weng, C. Fang, Z. Fang, B. A. Bernevig, and X. Dai, *Phys. Rev. X* **5**, 011029 (2015).
- [56] S.-M. Huang, S.-Y. Xu, I. Belopolski, C.-C. Lee, G. Chang, B. Wang, N. Alidoust, G. Bian, M. Neupane, C. Zhang, *et al.*, *Nature communications* **6**, 7373 (2015).
- [57] Y. Li, Y. Zhou, Z. Guo, F. Han, X. Chen, P. Lu, X. Wang, C. An, Y. Zhou, J. Xing, *et al.*, *npj Quantum Materials* **2**, 66 (2017).
- [58] J. Fang, C. Zhang, and Z. Ma, *Phys. Rev. B* **107**, 144512 (2023).
- [59] T. F. J. Poon and X.-J. Liu, *Phys. Rev. B* **97**, 020501 (2018).
- [60] C. Chan and X.-J. Liu, *Phys. Rev. Lett.* **118**, 207002 (2017).
- [61] Y. Zhang, S. Qin, K. Jiang, and J. Hu, *National Science Review* **10**, nwac121 (2023).
- [62] R. Giwa and P. Hosur, *Phys. Rev. Lett.* **127**, 187002 (2021).
- [63] R. Giwa and P. Hosur, *Phys. Rev. Lett.* **130**, 156402 (2023).
- [64] H. Wang, H. Wang, H. Liu, H. Lu, W. Yang, S. Jia, X.-J. Liu, X. Xie, J. Wei, and J. Wang, *Nature materials* **15**, 38 (2016).
- [65] M. D. Bachmann, N. Nair, F. Flicker, R. Ilan, T. Meng, N. J. Ghimire, E. D. Bauer, F. Ronning, J. G. Analytis, and P. J. Moll, *Science Advances* **3**, e1602983 (2017).
- [66] G. E. Volovik, *JETP letters* **93**, 66 (2011).
- [67] C. L. M. Wong, J. Liu, K. T. Law, and P. A. Lee, *Phys. Rev. B* **88**, 060504 (2013).
- [68] C. J. Lapp and C. Timm, *Phys. Rev. B* **105**, 184501 (2022).
- [69] A. Daido and Y. Yanase, *Phys. Rev. B* **95**, 134507 (2017).
- [70] N. F. Yuan, C. L. Wong, and K. T. Law, *Physica E: Low-dimensional Systems and Nanostructures* **55**, 30 (2014).
- [71] A. Chen and M. Franz, *Phys. Rev. B* **93**, 201105 (2016).
- [72] Y. Xie, X. Wu, Z. Fang, and Z. Wang, *Science China Physics, Mechanics & Astronomy* **67**, 127011 (2024).
- [73] C. Sun, S.-P. Lee, and Y. Li, *arXiv preprint arXiv:1909.04179* (2019).
- [74] T. Meng and L. Balents, *Phys. Rev. B* **86**, 054504 (2012).
- [75] X.-L. Qi, T. L. Hughes, and S.-C. Zhang, *Phys. Rev. B* **82**, 184516 (2010).
- [76] H. Chen, X.-J. Liu, and X. C. Xie, *Phys. Rev. Lett.* **116**, 046401 (2016).
- [77] N. Read and D. Green, *Phys. Rev. B* **61**, 10267 (2000).
- [78] P. Fulde and R. A. Ferrell, *Phys. Rev.* **135**, A550 (1964).
- [79] J. C. Y. Teo and C. L. Kane, *Phys. Rev. B* **82**, 115120 (2010).
- [80] A. Daido, Y. Ikeda, and Y. Yanase, *Phys. Rev. Lett.* **128**, 037001 (2022).